Supplementary Information for

Superconductivity beyond 500 K in a La-based superhydride

A. D. Grockowiak[*1,2], M. Ahart[3], T. Helm[4,5], W.A. Coniglio[1], R. Kumar[3], K. Glazyrin[6], G. Garbarino[7], Y. Meng[8], M. Oliff[1], V. Williams[1], N.W. Ashcroft[9], R. J. Hemley[3,10], M. Somayazulu[8], & S. W. Tozer[*1]

Correspondence to: Audrey.grockowiak@lnls.br, tozer@magnet.fsu.edu

This PDF file includes:

Figs. S1 to S20; S24
Table S21
Supplemental text S22-23

Fig. S1.

Pressure cells used and proposed for superhydrides synthesis and studies: left, Ø 38 mm UIC Mao-Bell DAC; center, DACs used for this study (B002 is assembled in the background with the parts of B003 in the foreground (the piston diameter is 5.38 mm and the total weight of the DAC is 12.88 g); right grouping, in foreground, plastic DAC that is typically used for our pulsed field work (ancillary parts to assist in loading shown in the background). With the diamond culets often being less than 70 μm for the superhydride work, the load necessary to generate the 1 to 2 Mbar pressures for synthesis of the superhydrides is quite small, which opens up the possibility of using this DAC[83] for superhydride studies in pulsed magnetic fields. It can be rotated at He-3 temperatures in pulsed fields and has no metal parts other than the electrodes, electrical leads and contacts and, in this case, the sample, thus minimizing eddy current heating in this high dB/dt environment.

Fig. S2.

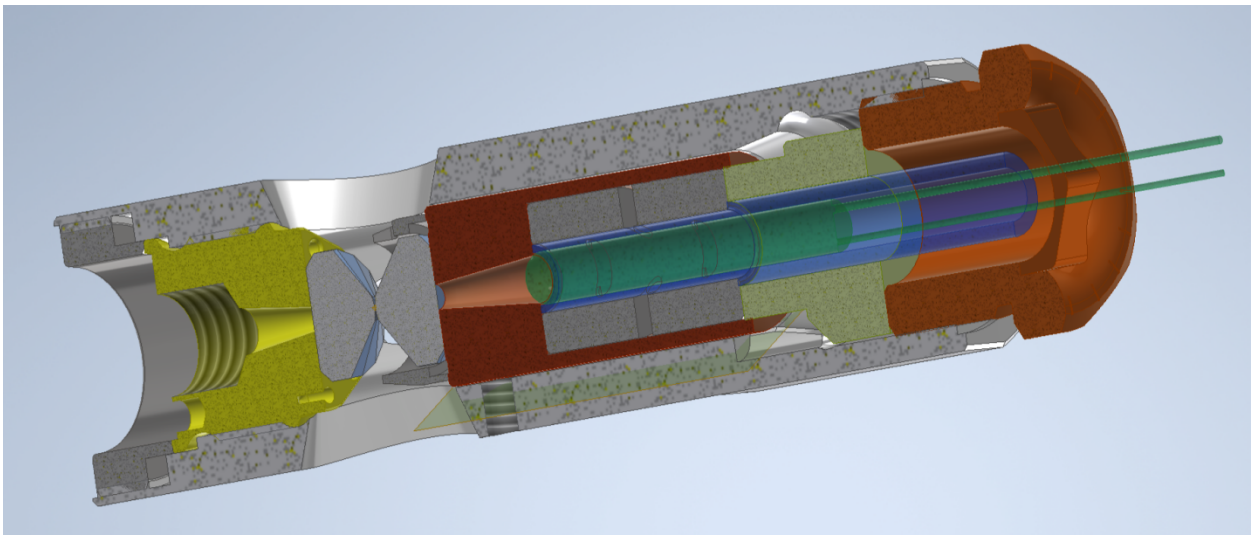

Model of the DAC used in these studies and shown in fig. S1: All metal parts of the DAC are made from Pascalloy (NiCrAl), but the parts are shown in different colors for clarity. The anvil with FIBed electrodes (external leads not shown) is attached to the endcap (yellow) to the left in this image while the anvil on the right is attached to a piston that is spring loaded. The gasket (not shown) and gasket table epoxied to the piston are electrically isolated from it and the rest of the DAC. Both anvils are secured using Stycast 2850FT blue/24 LV epoxy. The light green piece has three tabs that register with mating half cylinders in the body of the DAC to prevent the load nut (brown) to the far right from spinning the piston anvil when the load is increased so as to prevent damage to the sample, electrodes or anvils. The adaptor tube and the Pt-103 temperature sensor are shown inside the spring, in blue and green, respectively.

Fig. S3.

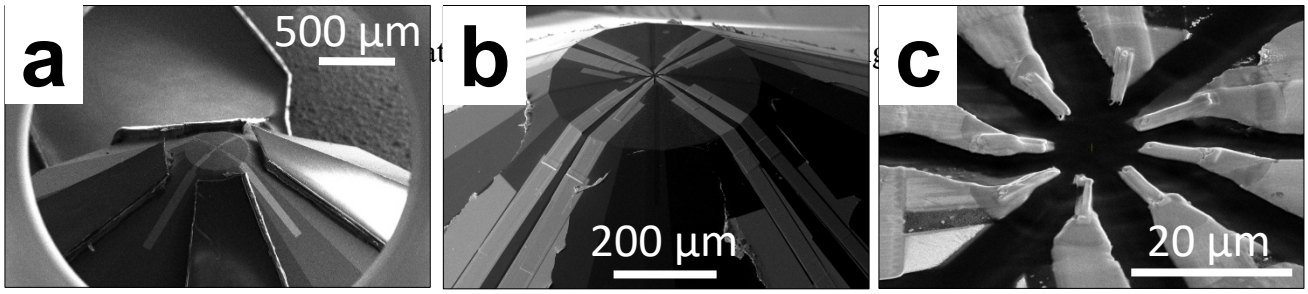

Images from the FIB processing: "a" shows the Kapton tape used to mask the stone prior to gold sputtering; "b" is the resulting AuPt overlay that has been defined with Ga; and "c" is an image of eight electrodes with tabs on top of one of the culets. Images taken at 52° off the orthogonal.

Fig. S4.

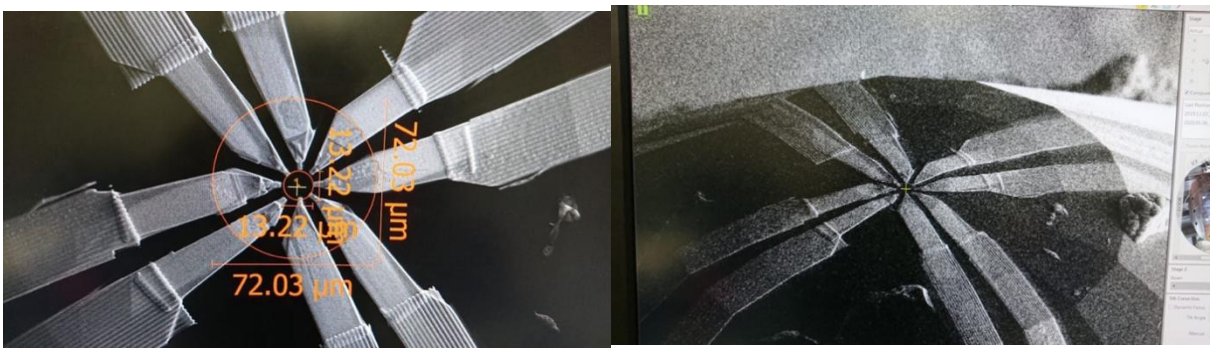

Two images of the FIB electrode fabrication on one of the anvils: left: a closeup of the Pt/Au/Pt electrodes is shown in which an overlay defines the edge of the 72 µm culet. The small tabs grown from the main electrodes encompass a 13 µm circle. Right: image shows the electrodes draped over the bevels and extending down the pavilion, where they are attached to the copper twisted pairs with Epotek H20E silver epoxy.

Fig. S5

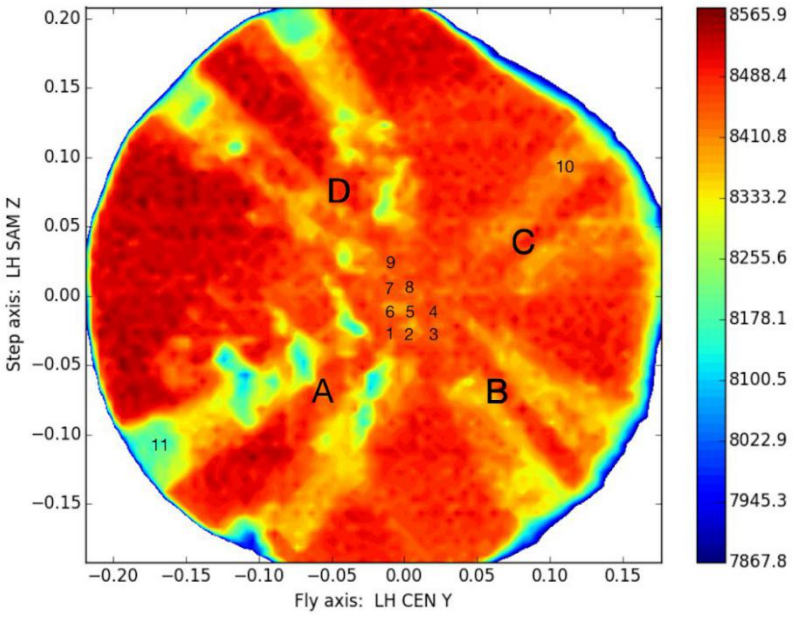

Image taken through the anvils of DAC B002 prior to the synthesis using X-ray transmission detected by a photodiode: the color scale indicates the X-ray transmission intensity, with red indicating greater transparency. The Pt/Au/Pt electrodes appear clearly in yellow. The letters indicate electrode pairs while the spots 1 to 9 indicate location of laser heating. The laser spot size was 20 μm in diameter. The laser was rastered in a 10 μm × 10 μm grid between spots 1 to 9, starting at 20% (41.5 W) of max laser power and then increased in 5% steps up to 70% laser power, or until coupling between laser and sample is observed to produce a temperature in the range of 1200 K. Coupling was characterized by a flash in the visual image of the sample and the temperature measured at the sample by a black body fit of the signal. The laser was pulsed 4 to 5 times at each spot.

Fig. S6

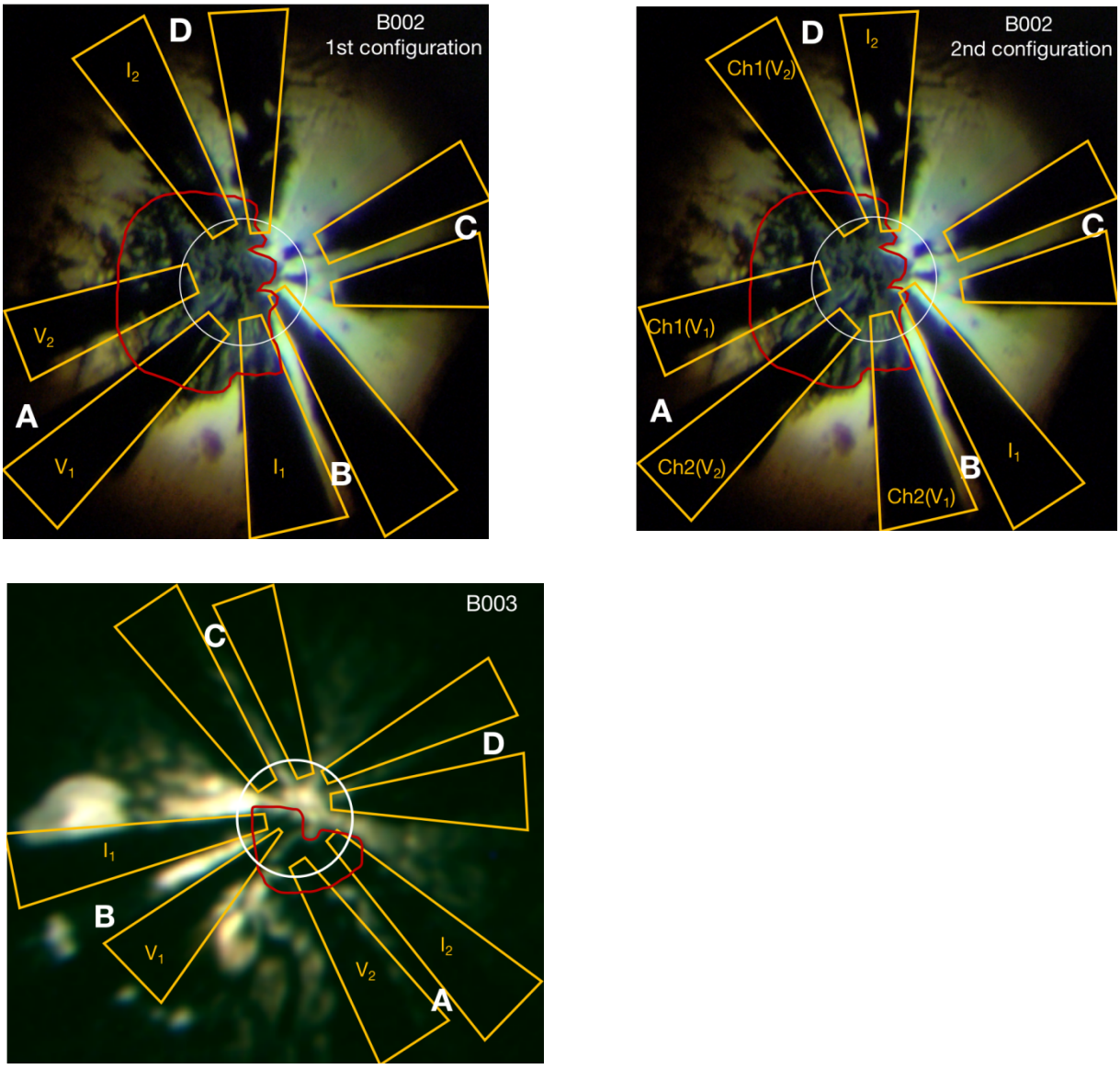

Transport electrodes configuration: top left: first electrode configuration for B002 used for the 294 K T_c measurement in the PPMS; top right, Channel 1 (Ch1) of the second electrode configuration was used for subsequent runs in the PPMS. Ch1 and Ch2 were also measured in the 41.5 T resistive magnet.
Bottom: electrode configuration for B003. The transparent area delineates the 200 μm outer edge of the first 8° bevel, which at these pressures is flat; the inner white circle indicates the perimeter of the 72 μm culet. All discussion of the diffraction data pertains to those collected in this area.

Fig. S7

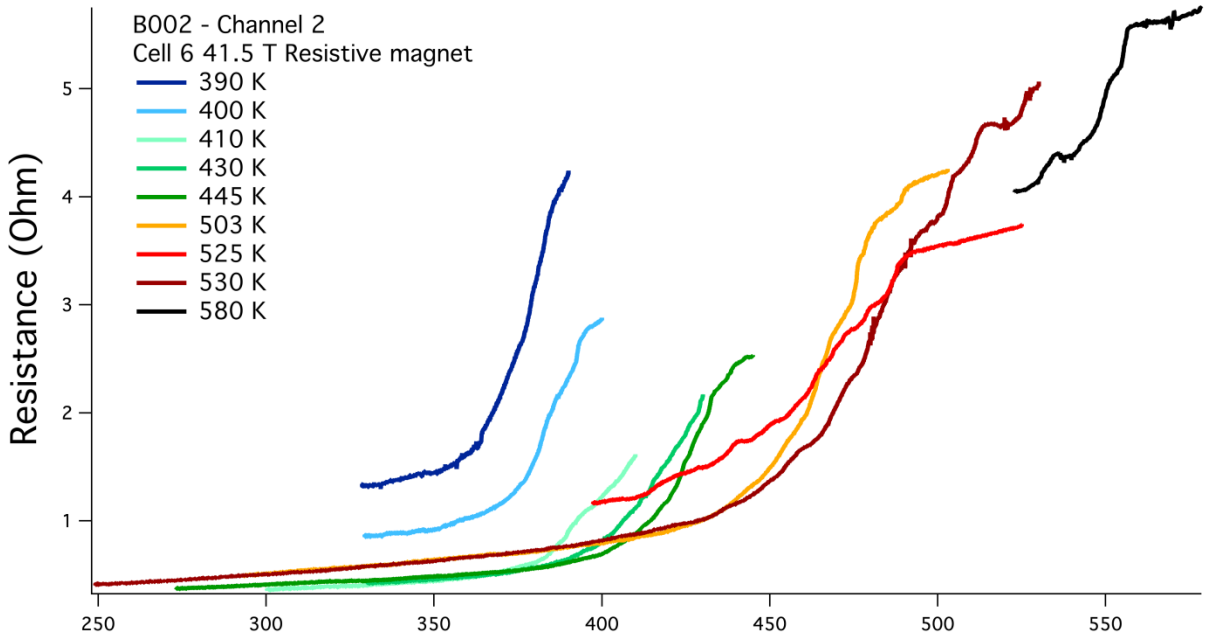

Cell B002, second electrode configuration: results obtained at 0 T for channel 2 that reproduce those observed in channel 1 shown in Fig 5 of the main text. Both sets of curves are the raw data obtained during cool downs. The heater failed during the 580 K run, which prevented us from obtaining data between 520 K and room temperature; however, the resistance of the sample at 300 K was the same as that for the other curves.

Fig.S8

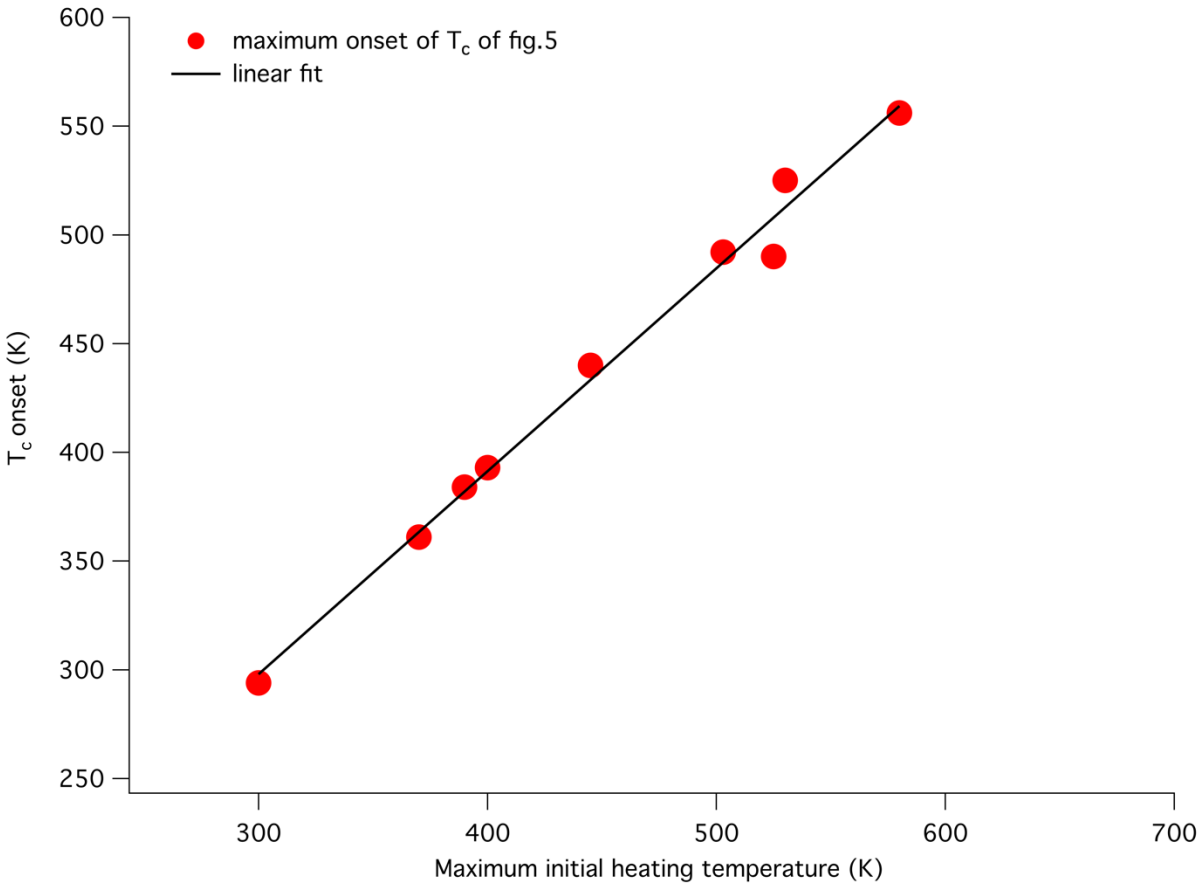

Cell B002: Onset of T_c upon cool down reported in fig.5 as a function of the maximum heating temperature. The linear fit (black line) between the T_c and heating temperature is a guide to the eye.

Fig.S9

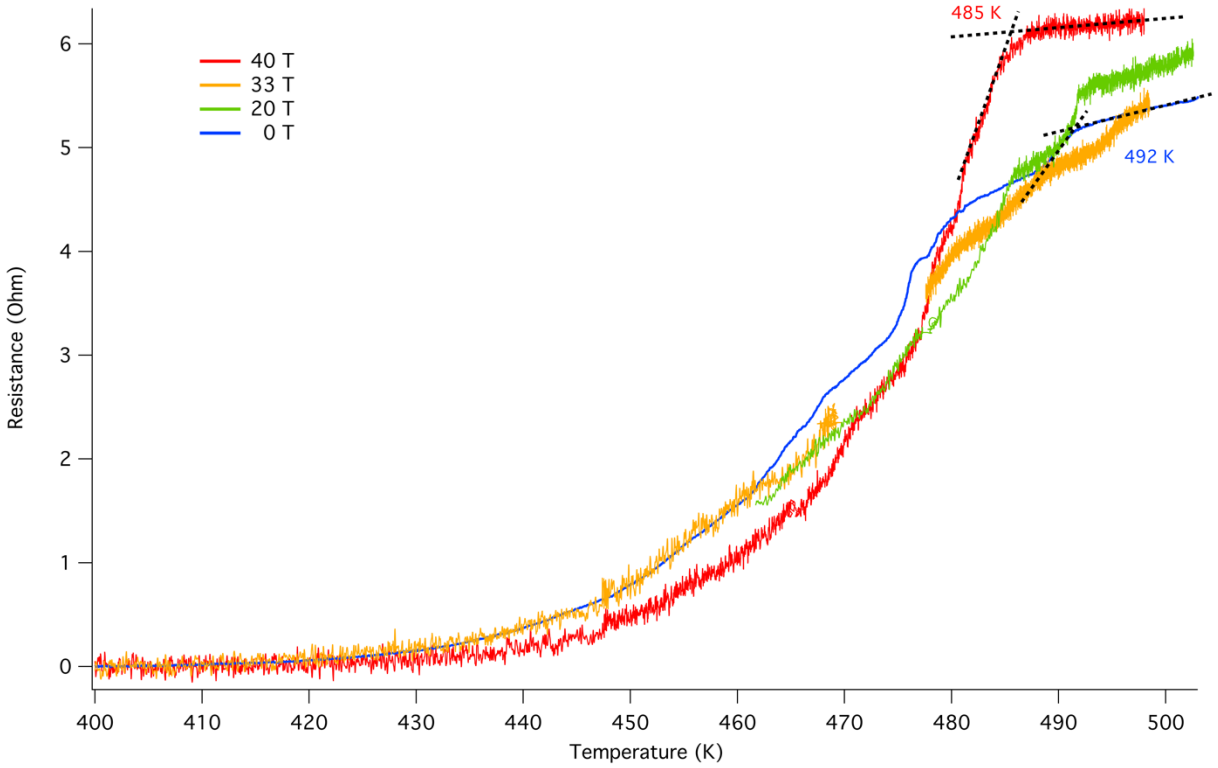

In-field cool-down traces for the 503 K family of curves for B002: R(T) showing cool down traces in static magnetic fields of 40 T, 33 T, 20 T and 0 T measured in that order for the family of 503 K curves. The temperatures in field are corrected for the magnetoresistance of the Pt thermometer (mechanically anchored to the interior of the DAC) (see fig. S1, S23 and S24), and a quadratic fit to the background was subtracted. The difference in signal over noise ratio between the zero-field and applied field traces arises from the vibrations generated by the cooling water flowing through the resistive magnet when in operation. The 0 T trace was recorded overnight and without the cooling water flowing. Although the onset of the transition shifts from 492 K at 0 T to 486 K at 40 T, the width of the transition at 0 T and the additional transitions appearing in the 20 T and 33 T curves hamper the interpretation. The incomplete nature of the chemical transformation precludes fixed-field temperature sweeps within any family of curves above 370 K. Indeed, the shift in the transition with each increasing temperature excursion and its multi-phase nature (fig. 5) suggests that the material is still evolving.

Fig. S10

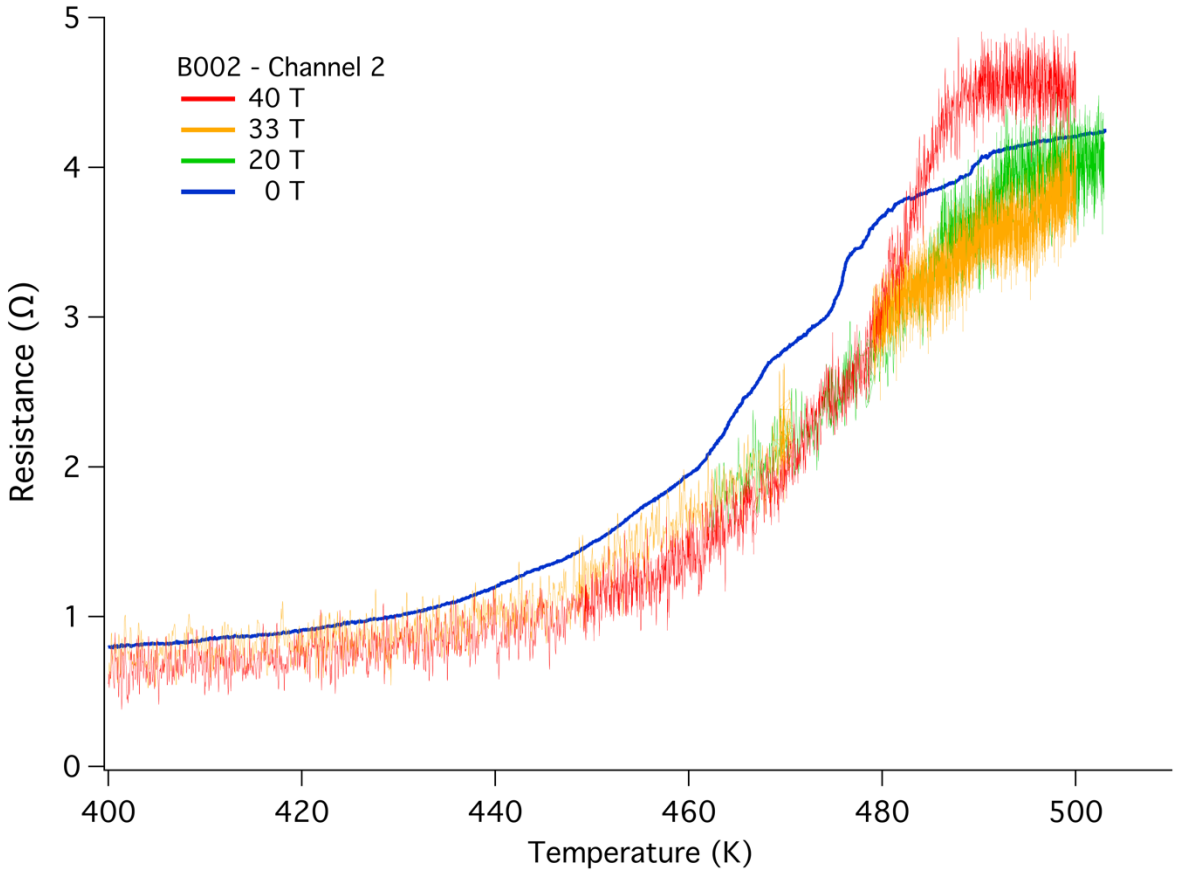

B002, second electrodes configuration: results obtained for channel 2 at different magnetic fields with the highest initial starting temperature of 503 K. The traces were measured at constant magnetic field of first 40 T, then 33 T, 20 T and finally 0 T. These results reproduced those shown in the main paper for channel 1. The noise level in the 40, 33, and 20 T traces is most likely caused by vibrations from the water flow in the magnet. The 0 T traces were carried out with the magnet and water cooling systems off.

Fig. S11

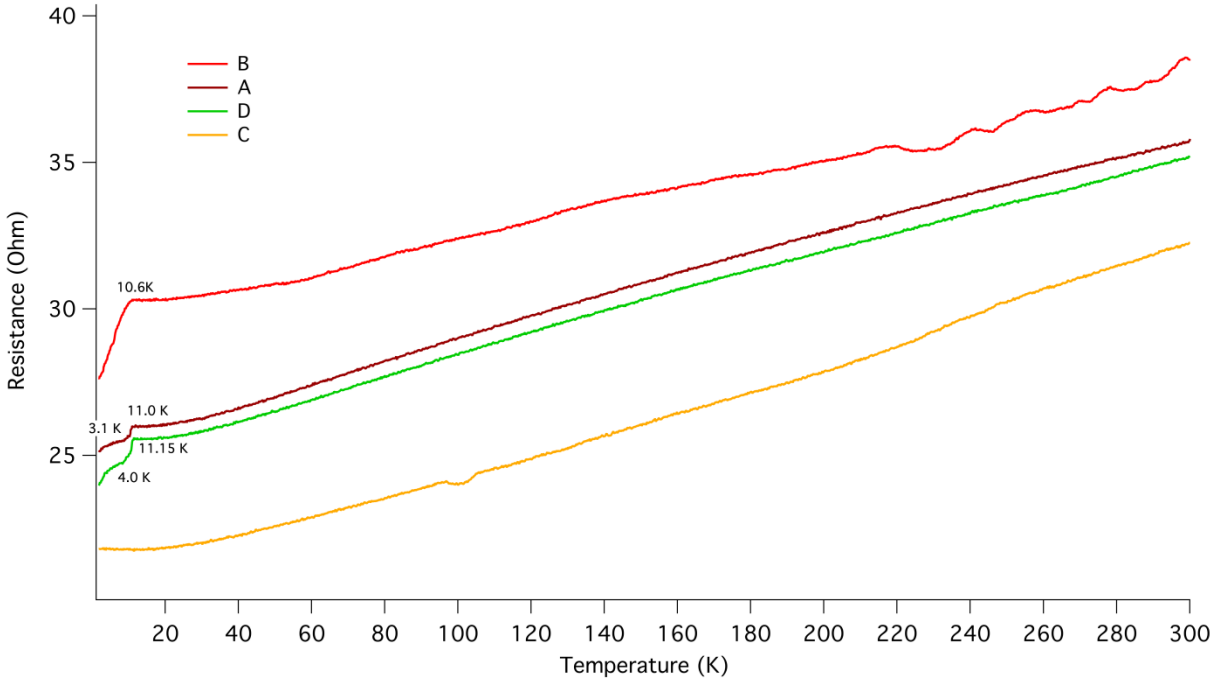

Comparison of various pseudo-4-probe measurements for B002 for the electrode pairs taken after the 580 K temperature excursion: electrode pair C is the open pair that only measures the MP35N gasket and the short between the leads caused by residual Au from the sputtering. However, the latter has a strong insulating behavior below 20 K, increasing in resistance from 120 Ω at room temperature to 1E6 Ω at 2 K (not shown). A, B and D exhibit superconducting transitions below 15 K with the slope of all curves in the normal state being comparable. The biggest contribution to the background at temperatures higher than 15 K is from the MP35N gasket (see fig. S12). Electrode pair B shows one strong superconducting transition at 10.6 K which is also observed at 11 K in A, and 11.15 K in D. It is most likely that these transitions are due to PtH that is also seen in the X-ray data[58]. We rule out a superconducting transition of elemental La as those T_c's would indicate a pressure well below 1 GPa[56]. These transitions could also be due to lower stoichiometry La superhydride, with the difference in T_c between the electrode pairs being due to compositional variations following an inhomogeneous synthesis, and/or the gradient of pressure across the culet. We attribute the transitions between 3 to 4 K to elemental La captured between the bevels (although the optical image of B002 does not show any La between the bevels of electrodes D) and/or unreacted La on the culet (also seen in the X-ray data).

Fig. S12

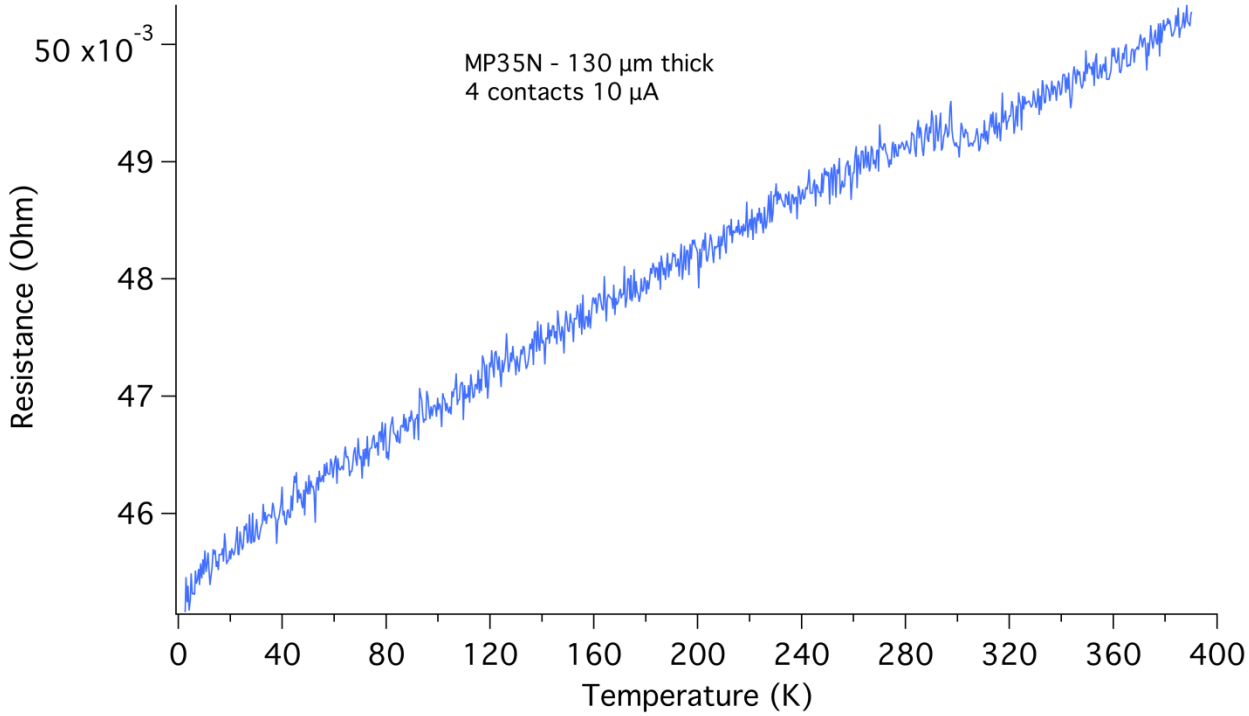

4-Probe measurement of MP35N: to rule out any transition originating from the gasket and to determine the background contributed by the short to the gasket, a 4-probe electrical transport measurement at 0 T and ambient pressure of a 135 µm strip of MP35N was made in the PPMS (this is the same material as used for the gasket). The kink around 300 K is due to a change in the temperature sensor used by the PPMS for the higher temperature range.

Fig. S13

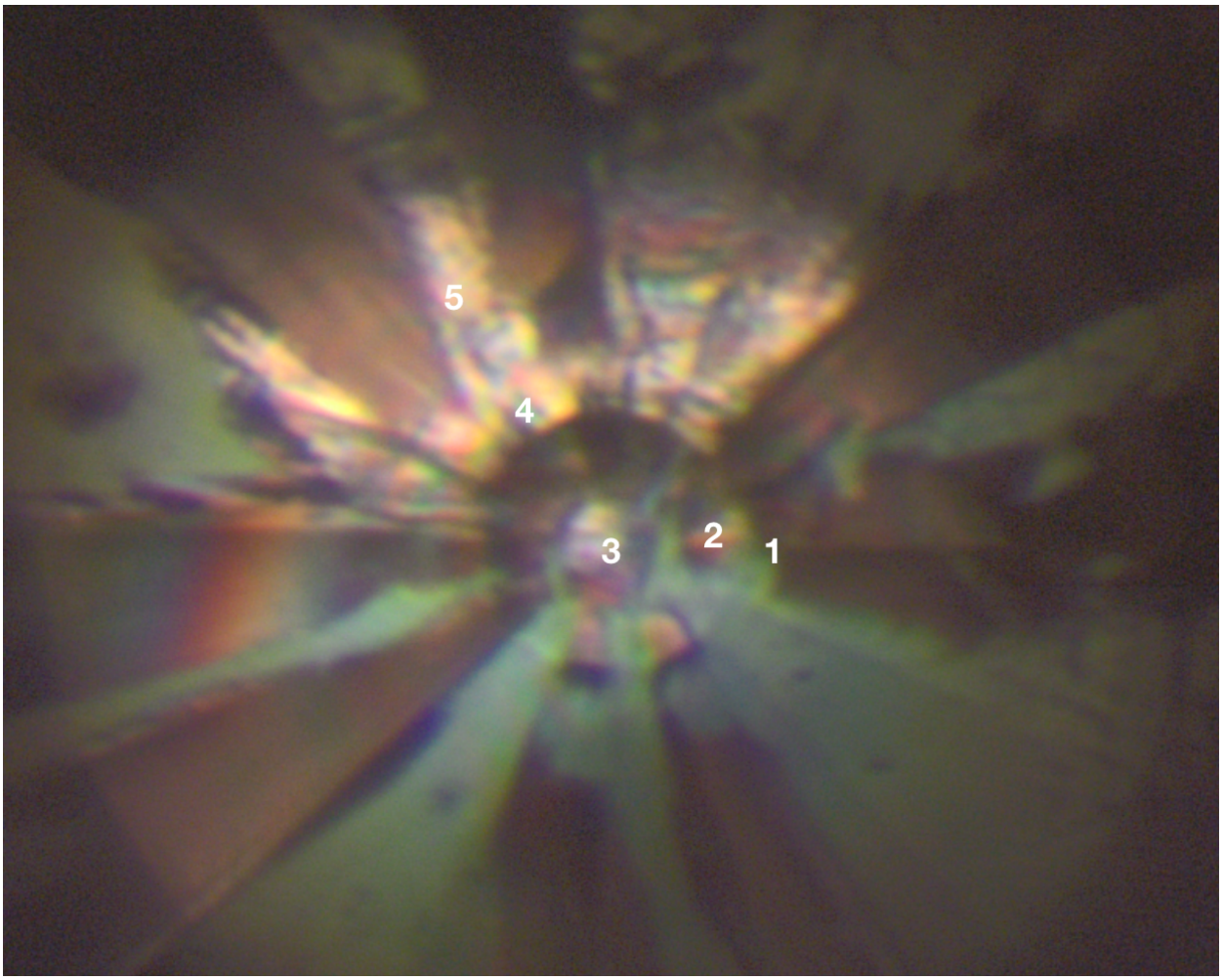

Micrograph of cell B002 taken at ESRF: pressure measured in July 2020 using the Raman edge of the diamond vibron measured with a 532 nm laser. The numbers indicate the positions where the pressure was measured: (1) 168 GPa, (2) 173 GPa, (3) and (4) 178 GPa, (5) 150 GPa. Position 3 is measured at the center of the culet. This value is consistent with the initial measurement done at HPCAT in March 2020 and those derived for the PtH, Pt, and La markers. Position 1, measured at the edge of culet, indicates a 5 GPa gradient of pressure across the culet. Position 5, in the bevel region and on the La, measured 150 GPa. This part of the sample was not laser heated.

Fig. S14

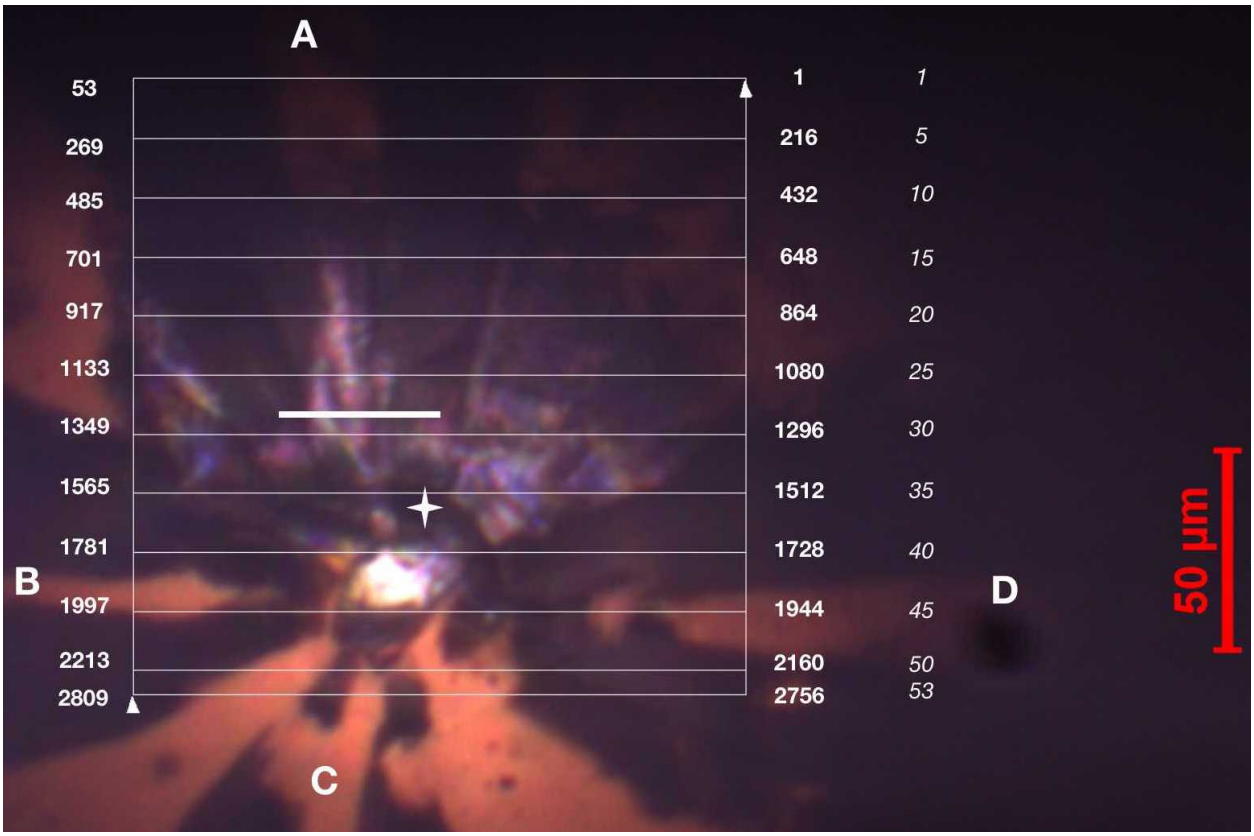

Additional XRD data: Grid of spectra numbers obtained at DESY on B002: 53 spectra were acquired on each of the 53 lines on a 3 µm grid. Spot size 3 × 3 µm^2. The white line is the approximate location of the spectra presented in S15. The star is the approximate location of the spectrum presented in fig. S17.

Fig. S15

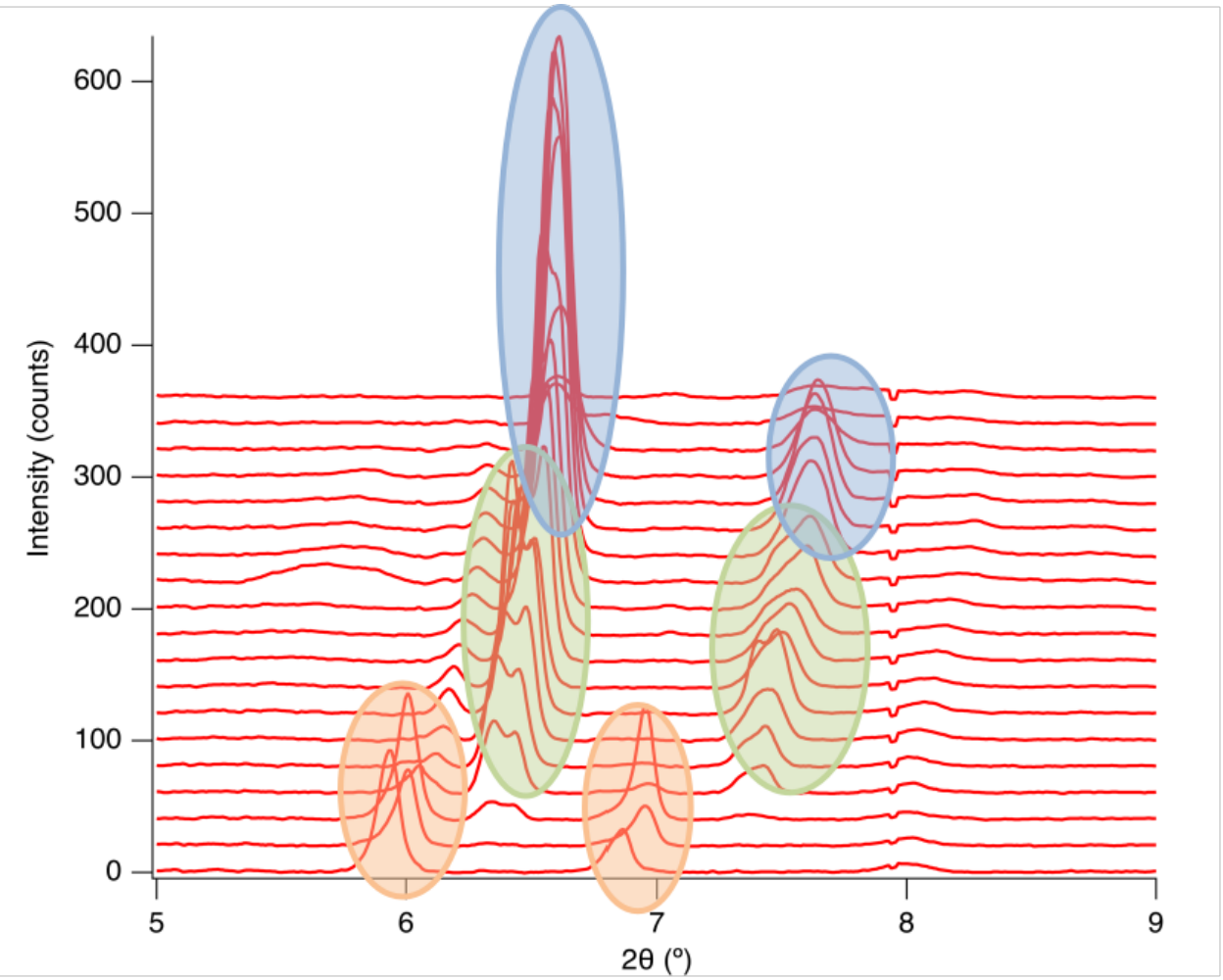

Additional XRD data: Spectra obtained on B002, line 27 (bottom to top spectra numbers 1385 – 1403). DESY X-Ray spot size: 3x3μm^2. Each spectrum is separated by 3 microns. Laser synthesis spot size: 9x9μm^2. We can resolve laser heating spots. Show clearly 3 different zones in the sample on that one line. This verifies the granular and inhomogeneous growth that results from using AB as a hydrogen source and laser heating done on a grid. It is clear that the voltage taps would sample not only the small bit with the very high superconducting transition, but also off-stoichiometric bits that gives rises to the broad, non-zero resistance that we observe.

Fig. S16

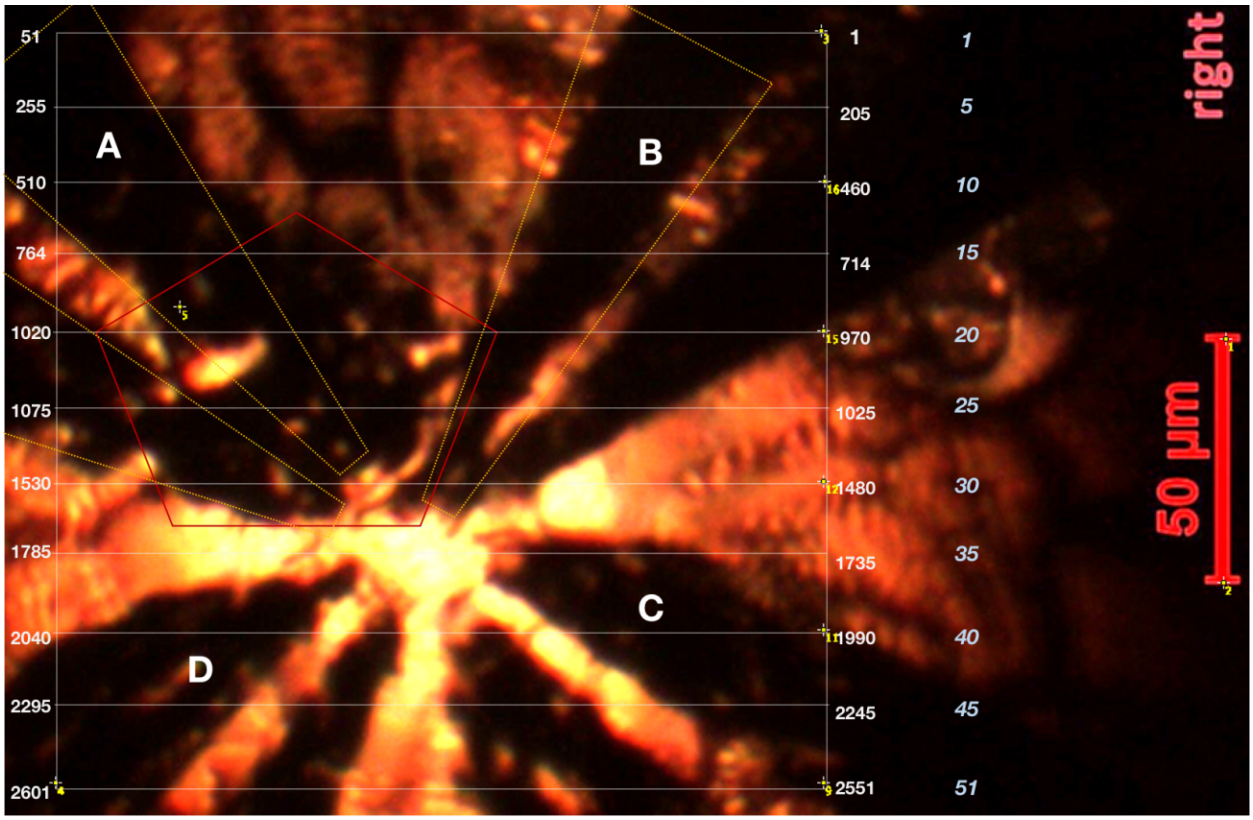

Additional XRD data: Grid of spectra numbers obtained at DESY on B003: 51 spectra on 51 lines. Approximate location of the sample indicated with a red pentagon. Electrodes pairs A and B were used for the transport measurements.

Fig. S17

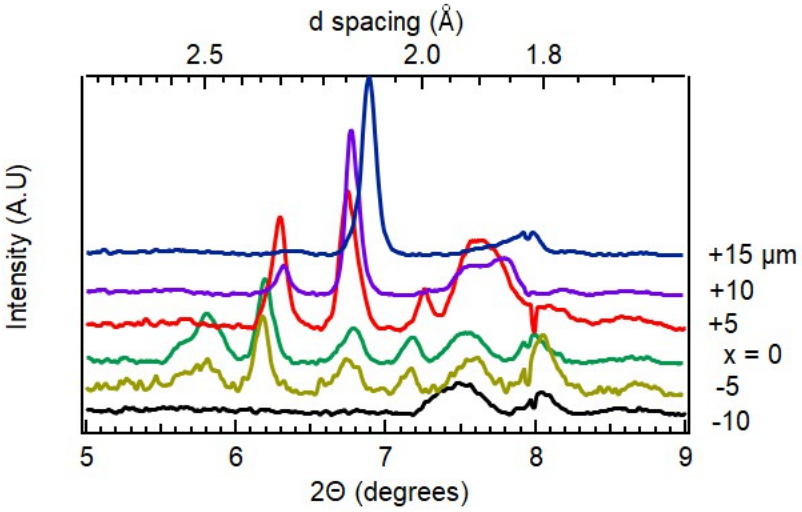

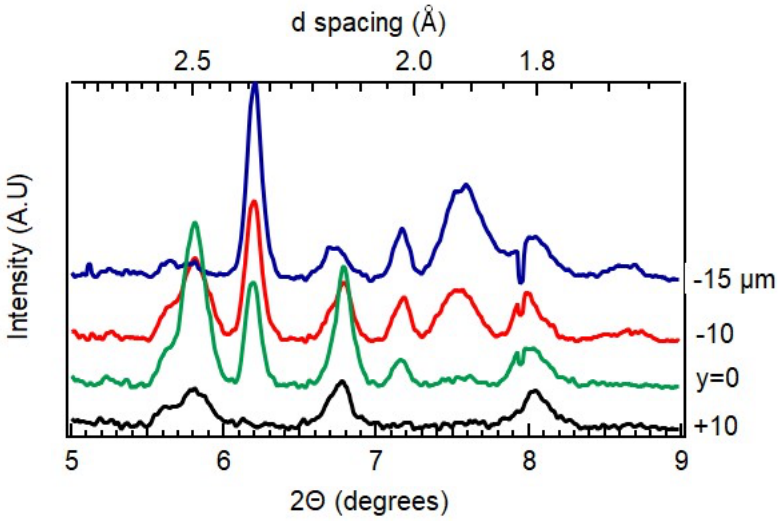

Diffraction patterns recorded as we move away (in both the scanned directions) from a point showing predominantly cubic (and rhombohedral) LaH_{10-x} in the sample. Initial assignment of peaks can be found in Ref 84. The sampling was coarsened (compared to the step used while recording the data - 3 µm by performing a 3 point boxcar averaging). This figure clearly shows that the synthesis occurs in localized regions in the sample which is also effectively corroborated by the contour plots below.

Fig. S18

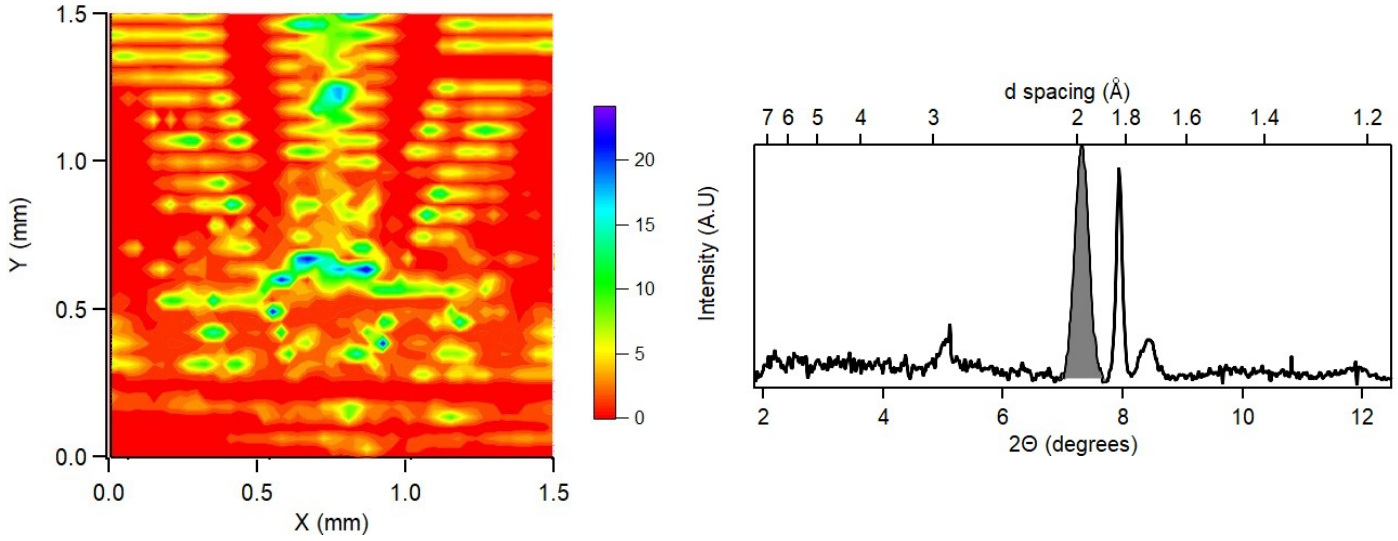

Additional X-ray data: Intensity contour of the Pt (111) diffraction peak over the full x-y scan. A representative diffraction pattern shows the relevant region in the observed patterns. The limits were relaxed to account for a systematic shift in the diffraction peak with varying pressure while ensuring that the accompanying lanthanum diffraction peak is not added in the integrated intensity. The electrodes and the central culet can be discerned. The axes are labelled in terms of the displacement from the starting point of the x-y scan (each step was 3 μm in both directions).

Fig. S19

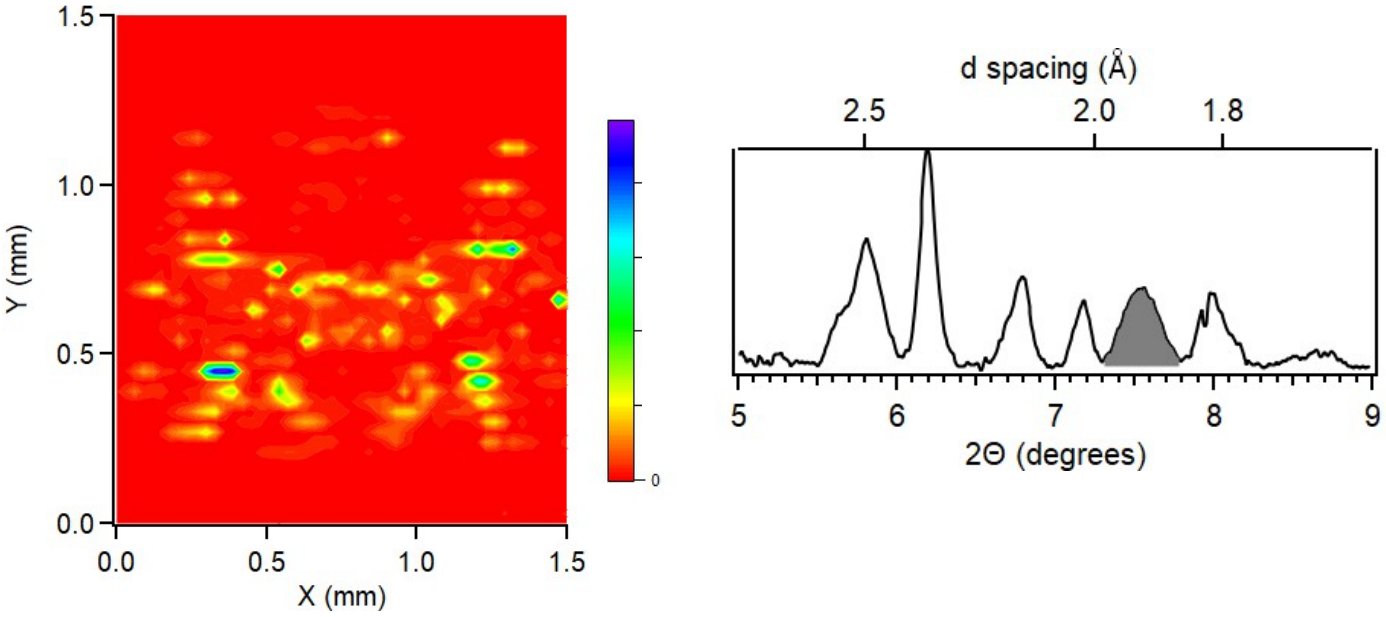

Additional X-ray data: Similar intensity contour obtained when the integration is over the lanthanum diffraction peak shown in a similar fashion above. However, the cross-talk from neighboring LaH_{10} and Pt diffraction peaks cannot be avoided effectively. Moreover, as can be seen in the optical micrograph (Fig. S6, S13 or S14), the spread of La is substantial and not confined to the culet.

Fig. S20

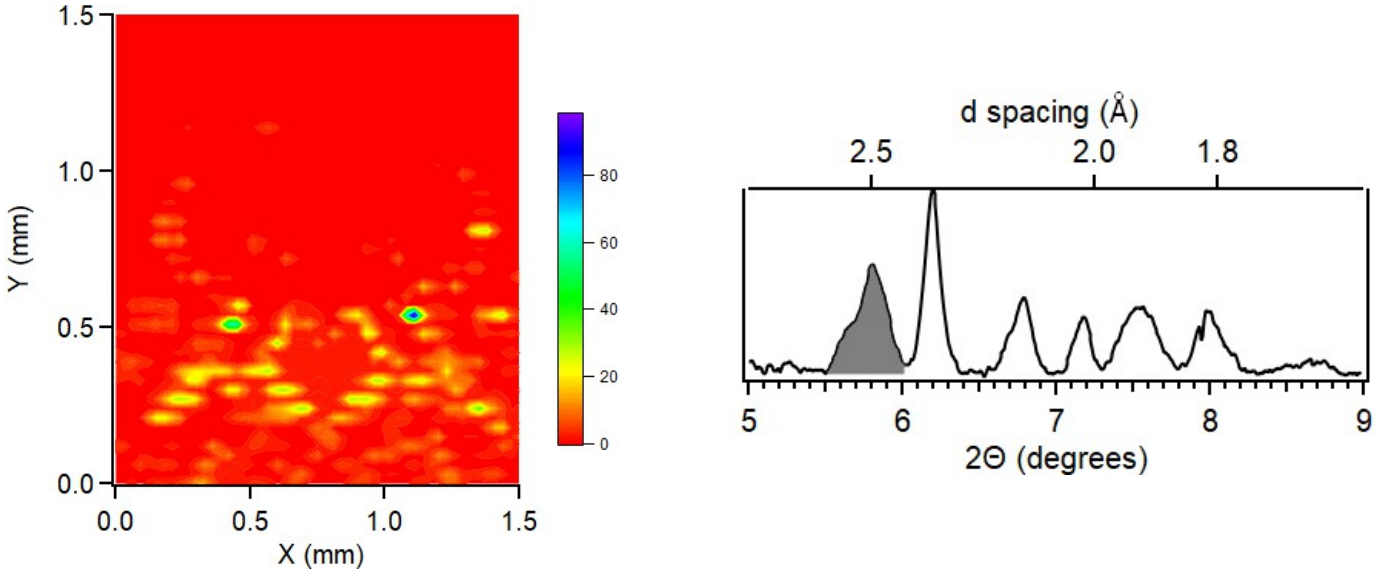

Additional X-ray data: Intensity contour obtained when the first observed diffraction peak from LaH_{10-x} (rhombohedral and cubic) is chosen (as shown in the representative pattern above). The overall disposition of the peak around the culet area which was heated during the synthesis is evident.

Table S.21

Datetime	Peak temperature (K)	Minutes within 10 K of peak
03/10/20	300	10

03/16/20	370	20
3/20/20 5:44 PM	381.7	22
3/20/20 8:02 PM	380.7	182
3/20/20 11:57 PM	390.1	26
3/21/20 1:30 AM	389.9	23
3/23/20 3:12 AM	385.4	87
3/23/20 2:43 PM	391.2	23
3/23/20 4:24 PM	392.3	83
3/23/20 7:31 PM	396.2	19
3/23/20 10:52 PM	391.2	19
3/24/20 8:02 AM	385.1	295
3/24/20 12:18 PM	385.1	69
3/24/20 2:19 PM	289	10
3/24/20 4:57 PM	27.1	23
3/24/20 9:40 PM	385.6	57
3/25/20 12:40 AM	404	13
3/25/20 12:59 AM	402.2	42
3/25/20 3:50 AM	400.2	62
3/25/20 9:05 AM	390.1	159
3/25/20 11:41 AM	406.4	123
3/25/20 2:03 PM	411.1	462
3/26/20 12:37 AM	410.3	89
3/26/20 6:51 AM	405.2	121
3/26/20 12:15 PM	432.6	240
3/26/20 3:08 PM	430.7	34
3/26/20 7:10 PM	445.4	70
3/27/20 8:57 AM	493	11
3/27/20 9:18 AM	500.5	52
3/27/20 1:46 PM	500.2	149
3/27/20 8:54 PM	503	54
3/27/20 11:09 PM	503.1	72
3/28/20 3:35 PM	530.7	38
3/29/20 3:12 PM	530	304
3/30/20 2:21 PM	530.1	278
3/30/20 5:19 PM	530.8	52
3/30/20 7:48 PM	525.4	58
3/30/20 11:10 PM	525.4	60
3/31/20 2:05 AM	525.4	69
3/31/20 5:54 AM	525.7	221
3/31/20 11:52 AM	525.7	58
3/31/20 2:43 PM	525.6	112

3/31/20 5:21 PM	480.9	14
3/31/20 8:04 PM	527.3	48
3/31/20 10:43 PM	525.4	60
4/1/20 1:39 AM	525.4	69
4/1/20 11:35 AM	320.3	128
4/2/20 12:52 PM	48.6	304
4/3/20 3:43 AM	524.8	45
4/3/20 10:19 AM	580	39

Journal of peak temperatures: to better establish the thermal pattern that led to the observed superconducting transitions, we provide a table of local maximum temperatures and the time spent at each one. We define a local maximum as the highest temperature reached before it is reduced by more than 10 K and the time as the continuous interval during which the temperature remained within 10 degrees of the stated peak, both before and after reaching that peak.

S22. Additional discussion relating to changes in pressure at high temperatures

In our experiments, we measured the sample pressure using the diamond Raman edge at room temperature. It was found to be 178 GPa in B002[82]. We did not measure the pressure while we heated the sample during conductivity measurements that were performed in our PPMS or in the higher field resistive magnets, however, we believe the pressure change was minimal during thermal cycles. We provided one argument as to why this is the case within the article. Here we provide a second to support our claim. We present two P-V-T equations of states. There are many papers on P-V-T equation of states of various materials, however, we choose these two as examples.

For the first example[85], we look at the P-V-T equation of state of ice-VII (fig. 2 therein): for a fixed volume (12 cm^3/mol), the pressure would change slightly more than 2 GPa if the sample temperature changes from 300 K to 600 K at 3 GPa (the initial sample pressure). However, for a volume of 8.6 cm^3/mol, the pressure would change less than 1.5 GPa for the same temperature range at 18.5 GPa (the initial sample pressure). Hence, the smaller volume indicates that the sample is at a higher pressure.

For the second example[86], please consider the P-V-T equation of state of iron (fig. 3 therein): for a fixed density (11 g/cm^3), pressure would change from 180 GPa to 210 GPa when sample temperature changes from 4000 K to 6000 K at 180 GPa (the initial sample pressure), a change of 1.5 GPa/per 100 K over this temperature range. This rate would be smaller for lower temperatures.

These two examples provide us with a very general conclusion - the thermal expansion of materials is small at very high pressure. Considering our 178 GPa sample, B002, where the volume changes will be extremely small, a temperature change from 300 K to 580 K would result in a change of several GPa at most at the maximum temperature. Therefore, we can safely say that the T_c changes during the thermal cycles due to the pressure change are minimal.

S23. Thermometer recalibration including the magnetoresistance

Contrary to the raw data obtained in the 41.5 T resistive magnet, the temperatures measured in the PPMS are internally corrected for field effects. In the 41.5 T resistive magnet setup, the temperature was measured via a Pt-103 sensor with a light press fit to the spring, 4 mm from the back of the anvil. The resistance of this sensor is measured by a Lakeshore 370, and converted to a temperature by using a calibration curve provided by the manufacturer at zero magnetic field and up to 800 K. As our results are resistance traces at fixed magnetic field, we had to take into account the magnetoresistance of the Pt sensor to recalculate the temperature. Two independent approaches, presented below, yield the same correction to within 0.15 K at 500 K.

Extrapolation of low field and low temperature magnetoresistance data:

The Pt sensor magnetoresistance (MR) was measured between 0 and 16 T in the PPMS at several temperatures between 240 and 390 K. The MR was fitted at each temperature by a linear and a

quadratic fit between 2 and 16 T. The temperature evolution of the coefficients of those fits was then fitted again with a linear and a quadratic fit. Those four fits generated were then extrapolated to 600 K and 41.5 T using the 0 T calibration curve and used to recalculate the temperature of the high field curves.

AI approach:

We bootstrapped this calculation by observing that at thermal equilibrium, the heater power and temperature are both stable. Due to the large thermal mass of the cell, it took about 100 seconds for the thermometer (and thermally coupled sample) to rise after adjusting the heater power. After that, additional slower factors made open loop stabilization an impossible task, particularly under time and magnet energy budget constraints. Controlled temperature ramps would have been impossible as well. Instead, we allowed the temperature controller to maintain the provided setpoint or ramp function while the platinum thermometer resistance increased upon increasing field. The controller reduced heater output to match the measured value to the setpoint. Therefore, the actual temperature of the thermometer was less than the setpoint and measured values.

The actual temperature must be obtained by examining the power output of the heater. The thermal lag between the heater and thermometer (sample) complicates matters, as it is an unknown function of time and temperature. To determine this function, we chose 22 sets of continuous temperature data that began from thermal equilibrium. In each case, we took the longest possible set of data, even when that meant concatenating data files into a quasi-continuously recorded stream, after accounting for the short gap between files.

There are two coupled problems to solve here. One is the equilibrium response curve between the heater and the thermometer, which is both nonlinear and also includes a contribution from the temperature of the surrounding cryogenic space. The other is the time-dependent portion. In our first attempt, we tried to solve the time-dependent portion by fitting poles and zeros to form a rational transfer function in the $s=j\omega$ domain, then applying the filter from an equilibrium point, but that left no mechanism by which to determine and adjust for nonlinearities in the overall heater-thermometer curve.

Instead, we employed a Deep Learning (DL) technique using fast.ai[87] as an interface to PyTorch[88] to model the entire nonlinear system. Deep Learning, colloquially called Artificial Intelligence, propagates inputs through layers of variables more numerous than the inputs themselves. Each layer includes a nonlinear function and a linear matrix operation. Coefficients are optimized iteratively on a portion of the data through a process called "training." Then, the model is compared to a non-intersecting portion of the data, called "validation." Input parameters were the heater output (0-100%) and VTI sample space temperature (242-319 K) Since a rational transfer function is not amenable to this technique, we provided the DL tool 40 taps of past values in both parameters with which it could form a sort of FIR filter. Tap delay ranged from 5 to 1310 seconds, which covers most of the response of the system.

Since the DL tool was solving two problems at once, we found that it simultaneously underfit the temporal problem while overfitting the equilibrium problem. Our result is very much dependent on an accurate, monotonic equilibrium response, so we fit Chebyshev polynomials to the

equilibrium result over the (VTI temperature, heater %) input space, then augmented the original input with that smoothed dataset. We ran the DL tool a second time to refine the temporal behavior while retaining the smooth equilibrium one. The resulting model could predict the temperature of the sample from the values and history of the VTI environment and the sample heater.

We applied the model to 14 upsweep magnet ramps of varying speeds and limits. Some included pauses at intermediate fields to verify the health of the magnet as well. During these pauses, we can observe that the slope of measured temperature vs. time is the same as the overall slope of the predicted temperature vs. time, thus verifying the accuracy of the DL model. Predicted temperatures from the model were adjusted up or down so they began at the zero-field indicated thermometer temperature. We then subtracted the thermometer data vs. time from the predicted temperature vs. time and plotted this "correction" trace as a function of field. The name correction is used because it may be added to magnetoresistive thermometer data to recover the actual temperature.

Observing (without surprise) that the correction traces seemed to be quadratic in field, we fit them with single-term $k_i B^2$ polynomials. Data at similar temperature ranges were grouped together for fitting, although we tried this several ways with no effect on the result. Finally, we considered the k_i polynomial coefficients as a function of temperature. Since magnetoresistance generally falls to zero at very large temperatures, we plotted them in inverse temperature and observed empirically quadratic behavior. The correction function (valid within 0.2 K tolerance for $300 <= T <= 530$ kelvin and $0 <= B <= 41.5$ tesla) for our Lakeshore Pt-100 platinum thermometer is $– 180\ B^2/T^2$.

The first magnetoresistance estimation yielded 4 possible corrections, the artificial intelligence approach gave a quadratic correction with field.
We plot below in figure S24 the second quadratic fit given by the first approach (labeled ADG), against the results given by the AI approach (labeled WAC). The results confirm each other within 0.15 K at 480 K and validate the correction.

Fig. S24

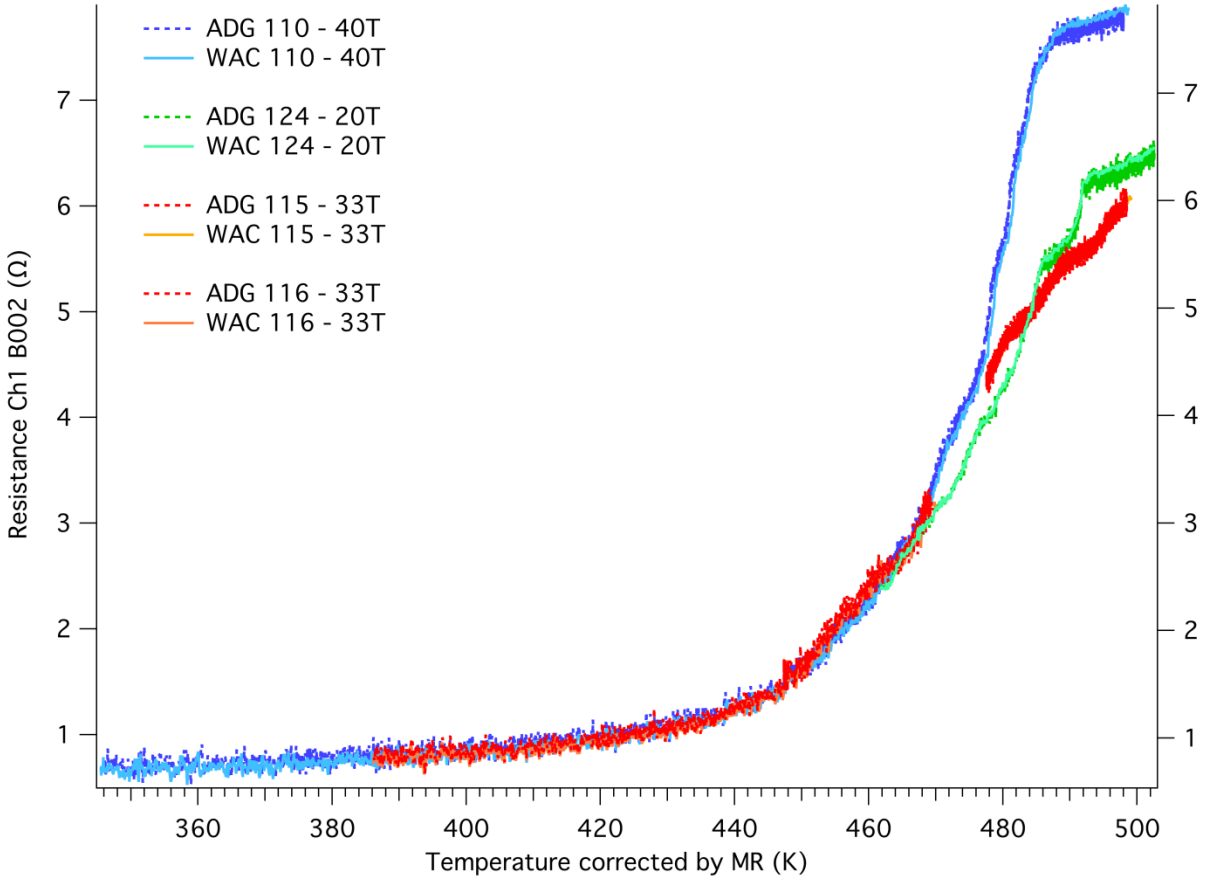

Comparison between the extrapolation (ADG) and the AI approach (WAC) for the magnetoresistance estimate correction. Both approaches yield the same result to within ±0.15 K at 480 K.